Journal of
Applied
Crystallography
ISSN 1600-5767

Received 22 November 2013
Accepted 17 December 2013

# A large-area CMOS detector for high-energy synchrotron powder diffraction and total scattering experiments

**Paula Macarena Abdala,[a] Henrik Mauroy[b] and Wouter van Beek[a]***

[a]Swiss–Norwegian Beamlines, ESRF, BP 220, Grenoble, 38043, France, and [b]Physics Department, Institute for Energy Technology, PO Box 40, Kjeller, N-2027, Norway. Correspondence e-mail: wouter@esrf.fr

A complementary metal-oxide semiconductor (CMOS) detector with an active area of 290.8 × 229.8 mm has been evaluated for X-ray scattering experiments at energies between 20 and 50 keV. Detector calibration and integration procedures are discussed in addition to the determination of the linearity, angular resolution and energy response of the detector in the context of its envisaged use. Data on reference compounds and samples with different crystallinity were collected and analysed with classical Rietveld and pair distribution function refinements. Comparisons with literature and high-resolution data from the same beamline demonstrate that the presented detector is suitable for crystallographic and total scattering experiments.



## 1. Introduction

Materials engineering and emerging technologies developments have benefitted from the use of synchrotron-based techniques as powerful tools for understanding the interplay between the structure of materials at atomic scales and their macroscopic properties. In particular, synchrotron X-ray powder diffraction (XPD) is extensively used to study the crystal structure as well as the microstructure of materials based on the analysis of the diffracted Bragg peaks. Time-resolved characterization provides crucial information about the functionality of the materials under operation and it requires highly penetrating radiation in addition to fast and efficient detectors.

Moreover, the study of complex materials exhibiting lack of long-range order, nanoscale structures or distorted local arrangements has become relevant since these materials show technologically interesting properties which are related to their degree of structural disorder (Egami & Billinge, 2003; Billinge, 2010). Total scattering and pair distribution function (PDF) analysis consider not only the Bragg reflections but also the diffuse scattering from a sample in order to look beyond the average structure, permitting an examination of the short- and intermediate-range order. To obtain sufficient resolution in real space it is important to collect data at high momentum transfer values $Q$ ($Q = 4\pi \sin\theta/\lambda$), with enough statistics. For this reason, high-energy photons at synchrotron beamlines together with large detectors are often combined for such purposes.

State-of-the-art direct-conversion single-photon counting detectors like the Pilatus (Kraft *et al.*, 2009) are not ideal for high-energy X-ray detection (>25 keV) as the active layer is made of silicon, leading to low sensitivity. Developments are ongoing to make high-$Z$ direct-conversion photon counting detectors (*e.g.* Ruat & Ponchut, 2012), but to date such devices are not available. The large detectors available on the market for high-energy detection almost exclusively make use of heavy scintillation materials [*i.e.* caesium iodide or gadolinium oxide (gadox)] to provide sufficient sensitivity. The optical photons produced in the scintillation process are collected with CCD-based, A-Si (amorphous silicon) or crystalline silicon CMOS (complementary metal-oxide semiconductor) detectors. CCDs (Labiche *et al.*, 2007) or A-Si (Chupas *et al.*, 2007) are typically being used for area detection XPD and total scattering experiments as well as slower scanning image plate systems. CMOS detectors have, so far, only been tested with low-energy single-crystal (Hasegawa *et al.*, 2009) or small/wide-angle X-ray scattering studies (Yagi & Inoue, 2007). Recently, commercial laboratory diffractometers have also been equipped with CMOS systems.

In this work, a large-area CMOS detector is evaluated for X-ray scattering experiments by measuring a series of different standards and samples, using energies in the range 20–50 keV. The linearity, energy response and resolution as a function of the sample-to-detector distance (SDD) are evaluated. Calibration and integration procedures are also discussed. In order to validate the use of this detector for powder diffraction and PDF experiments, samples with completely different crystallinity were studied by Rietveld and PDF methods. For convenience, this article is organized as follows: the 2923 CMOS detector description (§2); experimental setup, detector calibration and performance (§3); and, finally, crystallographic and total scattering performance (§4).

To the best of our knowledge, this is the first time that a CMOS detector has been employed for such purposes. All three detection systems (CCDs, A-Si or CMOS) have their advantages and disadvantages. Summarizing some of the

characteristics of CMOS detectors, one can say that they are fast and relatively low cost, they have a small pixel size, and they do not have image lag, even though the scintillator has a decay time. It is impossible to create a ranking between the three systems as their relative utility is highly dependent on the beamline, trade-offs and priorities in the envisaged type of experiments. Systematic efforts have been made to standardize performance comparisons of two-dimensional detectors for synchrotron radiation experiments (Ponchut, 2006). Such work is, however, beyond the scope of this article. Here we intend to validate the application of the CMOS detector for high-energy scattering experiments.

## 2. The 2923 CMOS detector

The Dexela-Perkin Elmer 2923 CMOS pixel detector tested is produced in large quantities and typically used in medical applications, such as tomosynthesis and computed tomography (CT), or industrial CT for detection of defects. The detector is air-cooled and consists of 3888 × 3072 pixels, where each pixel measures 74.8 μm$^2$ and is placed on a 75 μm pitch with an active area of 290.8 × 229.8 mm. The large surface area is achieved by tiling four smaller detectors together. There is a one pixel gap between each tile. The entrance window is made of a 1 mm-thick carbon fibre and low-density foam with a thickness of around 5 mm. The incoming X-rays are converted with a 250 μm-thick columnar CsI scintillator into optical photons. A fibre optic plate placed in between the scintillator and the CMOS sensor protects the sensor from the X-rays. The optical photons are converted into an electric signal by the CMOS chip. The sensor is equipped with amplifiers that can operate in two modes, changing the dynamic range (from 70 to 66 dB) and the sensitivity of the detector. The detector has a full dual cable camera link of 80 MHz capable of reading out all ∼12 million pixels 26 times per second with a 14 bit ADC resolution, resulting in a maximum frame rate of 26 Hz. The digital size of one full frame is about 24 Mbyte in Tiff format. The pixels can also be binned together as 1 × 2, 1 × 4 and 2 × 4 and the inverse, as well as 2 × 2 and 4 × 4. The smaller the number of pixels, the faster the readout will be. In 4 × 4 binning the detector runs at its maximum speed of 86 Hz.

## 3. Experimental setup, detector calibration and performance

The CMOS detector was mounted at the BM01B station at the Swiss–Norwegian beamline (SNBL) at ESRF in Grenoble (van Beek *et al.*, 2011). This station is equipped with two monochromators [a double-crystal monochromator (DCM) and a channel-cut monochromator (CCM)], a high-resolution powder diffractometer and an EXAFS setup. The two monochromators are mounted behind each other and can be shifted sideways in and out of the beam. The first DCM, normally used for EXAFS, has an energy range from 5 to 80 keV. The second CCM remains at a fixed angle at 24.797 keV and is used in combination with the high-resolution diffraction setup. The CMOS detector is mounted such that the same sample can be measured with both HRPD (high-resolution X-ray powder diffraction) and CMOS detection systems without moving it. The CMOS SDD was set at 184, 229, 289, 349 and 409 mm. The experiments were performed with X-ray energies of about 20, 25, 30, 35, 40 and 50 keV.

### 3.1. Dark current subtraction

CMOS sensors generate an image even when there are no X-rays present, a 'dark' image. Each pixel generates ∼8000 electrons per second of dark current at 313 K, but this value varies from pixel to pixel. It is, therefore, necessary to subtract a dark image from every exposed image (see Fig. 1). The dark current is very sensitive to variations in detector temperature occurring as a result of variations of, for instance, the ambient conditions. One can also see the effect of sample environmental cryogenic blowers placed close to the detector on the dark current. In this work, typically five dark and five X-ray exposures were alternated in order to have a valid dark image taken immediately before every exposure. *Fit2D* (Hammersley, 1998), running in batch mode, was used to average the dark and X-ray exposures and to subtract one from the other.

To streamline beamline operation, one would ideally like to avoid the sequence measurements of dark and exposed images and use an average of many dark images taken prior to an experiment. Active water cooling of the detector could improve the stability with the additional advantage of reducing the mean dark current (Graeve & Weckler, 2001), thus most probably avoiding the dark-exposure sequence during the experiments.

### 3.2. Angular calibration and integration

When including a two-dimensional detector for diffraction experiments in a beamline many different calibrations have to be performed. The wavelength, SDD and tilt parameters relative to the beam have to be defined. The wavelength and SDD correlate with each other and several procedures exist to reduce the degree of correlation (Hong *et al.*, 2012). In the

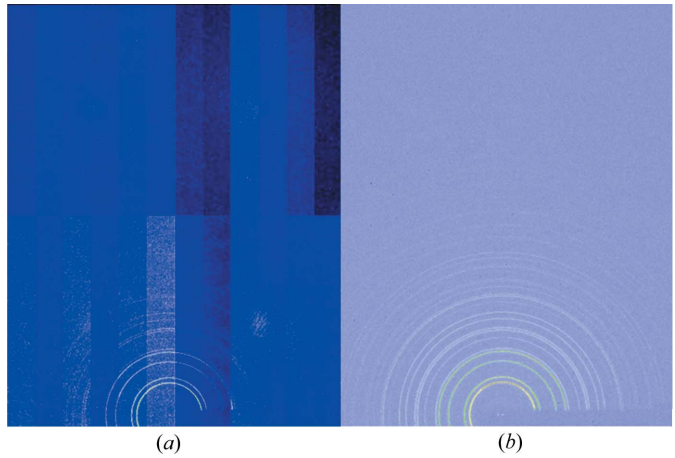

(*a*) (*b*)

**Figure 1**
(*a*) Raw image and (*b*) the same image with a dark image (not shown) subtracted, taken prior to the exposure.

combined HRPD–two-dimensional detectors setup this correlation can be totally avoided by measuring a standard with the two different detectors. Firstly, the wavelength is precisely refined with an Si powder standard (NIST SRM-640c) on the HRPD setup. Secondly, a sequence of dark and X-ray exposures is taken in exactly the same beamline configuration with the two-dimensional detector. The obtained wavelength is then used to determine the geometrical parameters (the five different SDDs, beam centres and tilts). *PyFai* software was used to refine the geometrical parameters. In Fig. 2, a typical calibration window is shown. It is important to note that, for obtaining a precise calibration, diffraction signals over the full surface of the detector *have* to be used (see Fig. 2). At 25 keV, 20 $LaB_6$ diffraction lines were used. Also note the diffraction on the first (333) harmonic at 75 keV inside the first diffraction peak on the (111) fundamental.

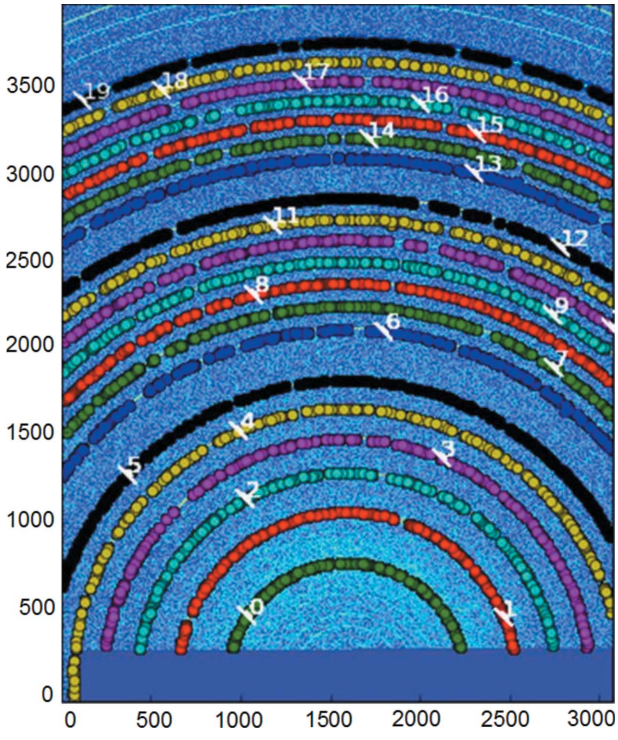


**Figure 2**
*PyFai* calibration procedure using the full surface of the detector. Note diffraction from the first harmonic at the bottom of the detector.

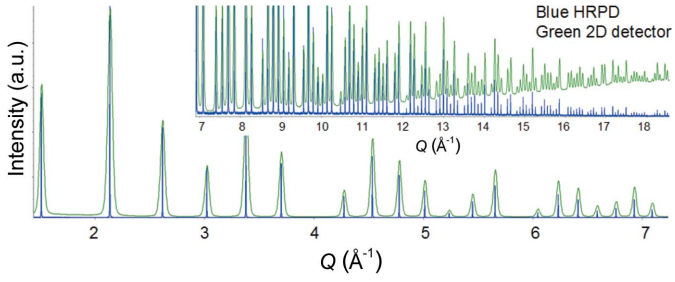


**Figure 3**
Normalized intensities plotted against $Q$ for data collected on $LaB_6$ using HRPD and the two-dimensional detector at 25 keV.

*PyFai* was also used for radial integration and solid angle and polarization corrections. Comparisons between HRPD and integrated two-dimensional data confirm that this procedure is reliable (see Fig. 3). Comparisons of refinements on both data sets, given in §4.4, also confirm this. The higher-energy experiments were performed after the geometrical calibrations at 25 keV. The DCM was used to set the X-ray energy and in *PyFai* only the wavelength and tilt parameters were refined as the beam centre and SDD remained fixed. This procedure again avoids any correlation between SDD and wavelength.

A library for image acquisition (LIMA) interface (Homs *et al.*, 2011) is currently under development for this detector and testing has started. This will allow easy integration into the beamline data acquisition software as well as on-line data treatment (dark image subtraction and radial integration) with *PyFai* (Kieffer & Karkoulis, 2013; Kieffer & Wright, 2013).

### 3.3. Angular resolution

The angular resolution as a function of SDD was characterized by fitting a split Pearson function to every peak in the $LaB_6$ diffraction pattern (in a 0.3 mm glass capillary) with *TOPAS-Academic* (Coelho, 2007) and summing the left and right side of the peak width to define the overall FWHM of the composite peak. At the shortest SDD of 184 mm the resolution was also determined for 40 and 50 keV. Characteristic parabolas are found when plotting the resolution $\Delta d/d$ as a function of $Q$ as shown in Fig. 4.

### 3.4. Linearity

The linearity of the detector response has been verified by using the 25 keV $LaB_6$ data at different SDDs. As the SDD decreases the angular resolution also decreases while the diffracted intensities remain the same. Effectively this implies that the same diffracted signal is spread out over more pixels

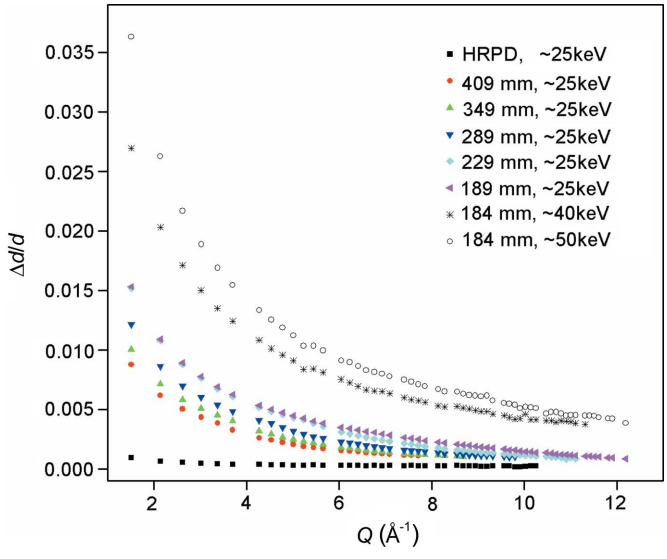


**Figure 4**
Detector resolution obtained on $LaB_6$ powder as a function of $Q$ for different SDDs and X-ray energies.

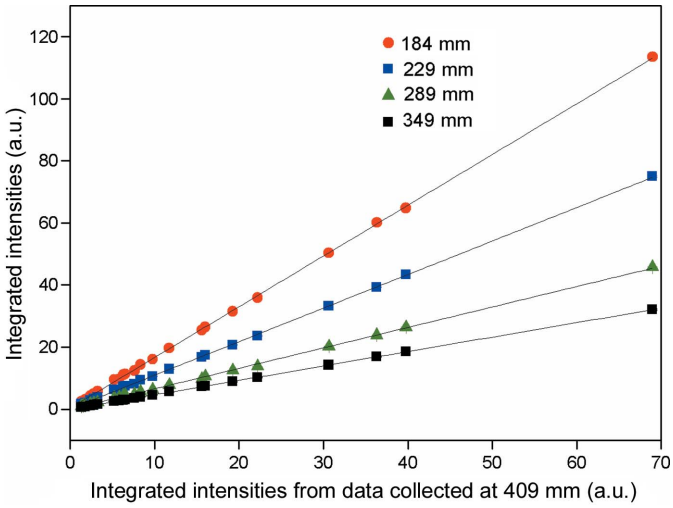


**Figure 5**
$LaB_6$ extracted intensities of shortest distances as a function of extracted intensities at 409 mm and linear regression fit to the data.

when the SDD gets shorter. The extracted intensities of the split-Pearson peak fits in *TOPAS* on the $LaB_6$ data as a function of distance were plotted against the furthest distance (409 mm) data (see Fig. 5). A simple linear regression fit $ax + b$ to the 409 mm data set provides $R^2$ values between 0.999964 for 349 mm and 0.999807 for 184 mm. The $R^2$ values for the other distances are in between these two numbers and indicate a satisfactory behaviour in the detector's linearity in the given environment.

### 3.5. Energy response

In order to investigate the energy response of the CMOS detector, XPD data on the $LaB_6$ standard were collected at different energies (~20, ~25, ~30, ~35, ~40 and ~50 keV). The extracted integrated intensity of each Bragg peak of the $LaB_6$ data, using the same procedure as for the angular resolution assessment, was divided with the extracted intensities from the 50 keV data. Fig. S1 (in supporting material[1]) indicates that there is, as expected, mainly a scale factor difference between the various data sets. Only at high scattering angles and low energies (20 and 25 keV) does a small deviation start to occur, suggesting that these intensities are somewhat underestimated. This is due to absorption either in the sample or in the entrance window of the detector and can be easily corrected for if needed.

## 4. Crystallographic and total scattering performance

### 4.1. Experimental

The standards and samples studied were lanthanum hexaboride ($LaB_6$, NIST SRM 660b), microcrystalline nickel powder (Sigma Aldrich 99.99%), AgI (Sigma Aldrich 99,999%), nanocrystalline yttrium-doped ceria (YDC) with a composition of $Ce_{0.8}Y_{0.2}O_{1.9}$ (Nextech Materials Ltd) and an amorphous $SiO_2$ glass rod (0.7 mm diameter). As a reference for the nanocrystalline YDC study, a microcrystalline $CeO_2$ powder has also been analysed.

All the powder samples were measured in 0.5 mm-diameter glass capillaries. XPD data of the empty glass capillary were collected under the same experimental conditions. The glass rod was measured without any sample container. The data were collected at two different wavelengths with the Si(111) DCM at ~40 keV [just below the absorption Ce *K*-edge (40.4 keV) in order to reduce fluorescence in cerium-containing samples] and at ~50 keV. The wavelengths were determined at 0.30988 Å (40.0104 keV) and 0.24720 Å (50.1554 keV) while the $Q_{max}$ values were 20 and 24.5 $Å^{-1}$, respectively. Peaks of the third harmonic (at ~75, ~120 and ~150 keV) were also identified at low scattering angles (see also Fig. 2). The suppression of the harmonic was performed by detuning of the second crystal of the DCM to 65% transmission. The calibration and azimuthal integration procedure of the two-dimensional data were performed as previously described. The SDD was set to 183.8 mm, coming from the first calibration with a known wavelength from the HRPD data set, and was kept fixed during all the measurements. The ESRF synchrotron was run in multi-bunch mode (maximum electron current 200 mA). The beam size was set by slits to 0.4 × 0.4 mm using unfocused 'parallel' X-rays. The flux on the sample was about $1.2 \times 10^9$ photons per second per 200 mA at 20 keV and $2.35 \times 10^8$ photons per second per 200 mA at 50 keV, the flux at the other energies lies in between. An *ad hoc* shielding was placed near the sample in order to reduce the background scattering from the air and a tungsten carbide beamstop was placed between the sample and the detector. Different integration times were achieved by averaging 2–500 images. The high-sensitivity mode of the detector was used for all experiments. The exposure time for each image was adapted to stay within the dynamic range of the detector, between 1 and 5 s depending on the sample. Sequences of five X-ray images and five dark images were collected as described in the previous section.

### 4.2. Rietveld analysis

Rietveld refinements were performed on $LaB_6$ and Ni data collected on the CMOS detector and the HRPD data set by using the *FullProf* (Rodriguez-Carvajal, 2001; http://www.iucr.org/__data/assets/pdf_file/0019/21628/cpd26.pdf) program. The crystal structure published by Korsukova *et al.* (1984) (space group $Pm\bar{3}m$ with La in the 1*a* and B in the 6*f* positions) was used in the refinements for $LaB_6$, and for the refinement of the Ni data the structure by Rouquette *et al.* (2008) (space group $Fm\bar{3}m$ with Ni in the 4*a* position) was used.

### 4.3. Pair distribution function analysis

The pair distribution function $G(r)$ indicates the probability of finding two atoms separated by a distance $r$, including those pairs that may deviate from the average long-range structure.

[1] Supporting information is available from the IUCr electronic archives (Reference: HE5639).

**Table 1**
Results for Rietveld refinement of $LaB_6$.

$\lambda = 0.24720$ Å and SDD = 184 mm for the CMOS detector, and $\lambda = 0.505411$ Å for HRPD.

| Detector | CMOS | HRPD |
|---|---|---|
| Unit-cell parameter $a$ (Å) | 4.1576 (2) | 4.15701 (2) |
| Atomic position of boron ($x_B$) | 0.1986 (8) | 0.1997 (6) |
| $u_{iso\text{-}La}$ (Å$^2$) | 0.0051 (1) | 0.0054 (1) |
| $u_{iso\text{-}B}$ (Å$^2$) | 0.0038 (1) | 0.0038 (1) |
| $R_p$† | 3.6 | 8.5 |
| $R_{wp}$† | 2.7 | 10.8 |
| $R_{exp}$† | 1.8 | 9.0 |
| $R_{wp}/R_{exp}$† | 1.5 | 1.2 |

† Conventional reliability factors in the Rietveld analysis.

In contrast to crystallographic methods, the PDF does not need any assumption on the periodicity. The atomic PDF, also called $G(r)$, is defined (Egami & Billinge, 2003) as

$$G(r) = 4\pi r[\rho(r) - \rho_0], \quad (1)$$

where $\rho(r)$ is the atomic pair density, $\rho_0$ is the average atomic number density and $r$ is the radial distance. It is obtained experimentally by the Fourier sine transformation of the total structure function $[S(Q)]$:

$$G(r) = (2/\pi)\int_0^\infty Q[S(Q) - 1]\sin(Qr)\,dQ. \quad (2)$$

In order to evaluate the data quality or detect any background problems, the so-called reduced structure function $F(Q)$ is a useful representation since it provides the $Q$-weighted data. It is defined as

$$F(Q) = Q[S(Q) - 1]. \quad (3)$$

The real-space resolution is directly related to the maximum of the momentum transfer measured, $Q_{max}$. A key experimental criterion for obtaining the quantitative PDF is to be able to measure the total structure function $S(Q)$ to large values of $Q_{max}$ with sufficient statistics. $Q_{max}$ is defined by the experiment geometry (SDD and size of the detector) and the wavelength of the incident beam.

In order to obtain the $F(Q)$ and $G(r)$ functions the processing of the data was performed by the program *PDFgetx3* (Juhás *et al.*, 2013). Refinements of the structural models for Ni and nano-YDC against $G(r)$ were performed with the program *PDFgui* (Farrow *et al.*, 2007).

### 4.4. Results and discussion

**4.4.1. Rietveld analysis on $LaB_6$.** Fig. 6 shows the Rietveld refinement plot of the $LaB_6$ data collected with the CMOS detector at 0.24720 Å (50.1554 keV). The results are summarized in Table 1 and compared with the respective values obtained from the analysis of the HRPD data at 0.505411 Å (see Fig. S2); the FWHM of the 110 reflection was 0.11° ($\Delta d/d = 0.3$) and 0.012° ($\Delta d/d = 0.009$), respectively. The refined parameters from both data sets are consistent and in good agreement – within the errors – with literature values (Booth *et al.*, 2001).

**4.4.2. PDF and Rietveld analysis on nickel powder**. Ni powder has been widely used as a benchmark sample for PDF

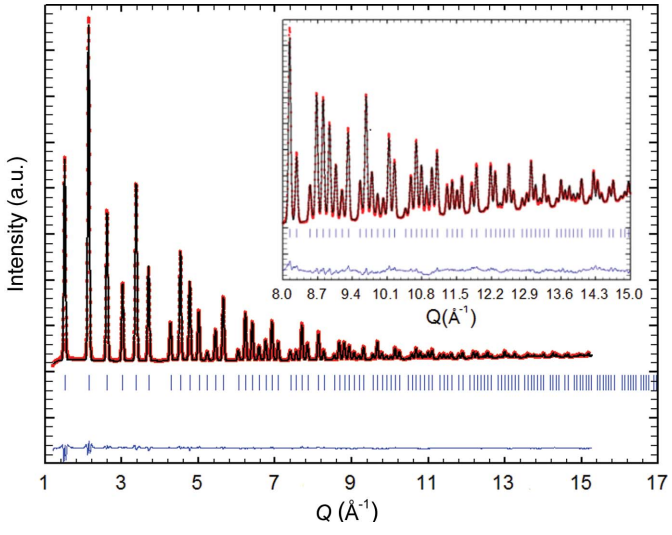


**Figure 6**
$LaB_6$ Rietveld refinement on data collected at $\lambda = 0.24720$ Å with the CMOS detector. The inset is an enlarged view of the data at high $Q$ values.

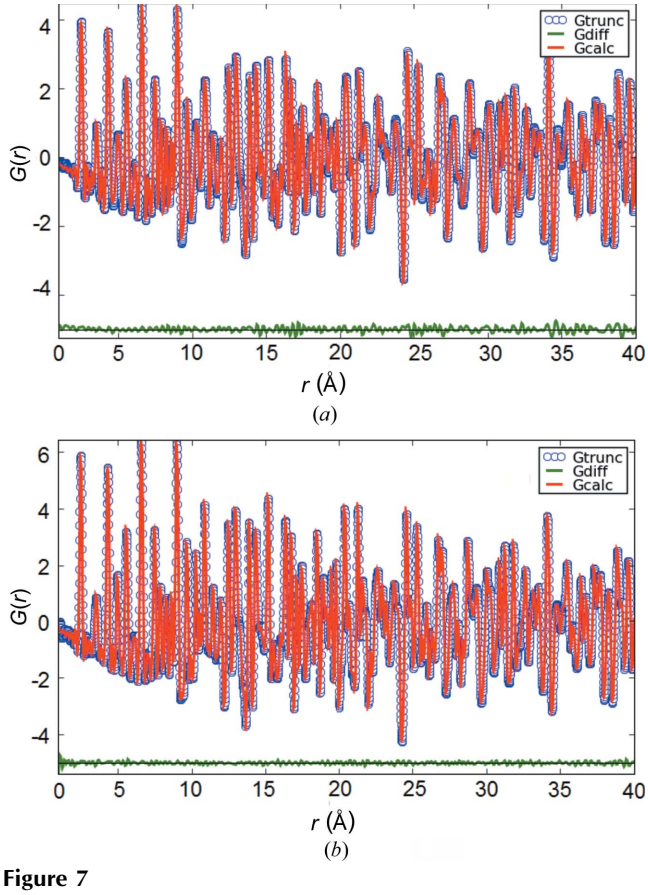


**Figure 7**
The experimental (empty blue circles) and the calculated PDF (solid red line) of nickel data collected at wavelengths of (*a*) 0.30988 Å and (*b*) 0.24720 Å. The differences between the calculated and the experimental data are shown below offset (solid green line) in each plot.

**Table 2**
Summary of the refinement parameters for nickel powder.

*Fullprof* used for conventional Rietveld refinement and *PDFGui* used for the real-space refinement.

| Analysis | Rietveld analysis | | | PDF analysis | |
|---|---|---|---|---|---|
| Wavelength (Å) | 0.505411 | 0.30988 | 0.24720 | 0.30988 | 0.24720 |
| Cell parameter $a$ (Å) | 3.52412 (1) | 3.52359 (1) | 3.52495 (1) | 3.5247 (2) | 3.5249 (2) |
| $Q_{min}$–$Q_{max}$ (Å$^{-1}$) | 2–14 | 2–14 | 2–14 | 0.5–20 | 0.5–24.5 |
| $u_{iso}$ (Å$^2$) | 0.0048 (1) | 0.0039 (2) | 0.0039 (2) | 0.0045 (2) | 0.0044 (1) |
| $Q_{damp}$† | – | – | – | 0.020 | 0.025 |

† Gaussian dampening envelope due to limited $Q$ resolution.

developments using neutron or X-ray sources (Chupas *et al.*, 2007, 2003; Juhás *et al.*, 2013; Neuefeind *et al.*, 2012). For this case, we have performed conventional Rietveld (in reciprocal space) and PDF (in real space) refinements on data collected at two different wavelengths (0.30988 and 0.24720 Å) using the CMOS detector. As an independent reference, a powder diffraction pattern collected on the HRPD detector was also analysed by conventional Rietveld refinement, yielding accurate cell parameters and thermal factors.

The results of the analysis are given in Table 2 and the Rietveld refinement plots are presented in Fig. S3. The experimental PDFs were obtained by Fourier transformations of the total scattering structure functions $S(Q)$ up to 20 and 24.5 Å$^{-1}$ for 0.30988 Å (40.0104 keV) and 0.24720 Å (50.1554 keV), respectively. The experimental $G(r)$ functions are plotted in Fig. S4. Figs. 7(*a*) and 7(*b*) show the experimental and calculated $G(r)$ functions of the data collected at the two different wavelengths with a total acquisition time of 300 s. The Ni $G(r)$ shows minimal systematic errors, observed as the small ripples before the first PDF peak at about $r$ = 2.4 Å. The lattice parameters and the displacement factors obtained from the PDF analysis reproduce adequately the expected values given by Rietveld analysis performed on the HRPD and the CMOS detector data as well as the literature values (Juhás *et al.* 2013). The $R_w$ values of the PDF refinement were 0.4 and 0.3 for the data collected at the lower and higher energy, respectively. These values cannot be directly compared with the Rietveld $R_w$ values. Table 2 reports the $Q_{damp}$ value obtained in the refinements, which represents the Gaussian dampening envelope due to limited $Q$ resolution.

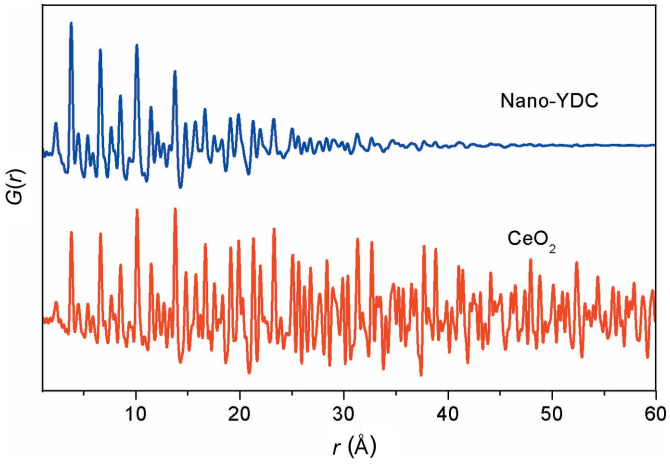


**Figure 8**
Experimental PDFs for nanocrystalline YDC and microcrystalline $CeO_2$.

**4.4.3. PDF analysis on nanocrystalline yttrium-doped $CeO_2$.** As an example of a nanocrystalline material, yttrium-doped ceria with an average crystallite size of about 4 nm (as determined from the Scherrer formula on the HRPD data) was analysed by the PDF method. Nanostructured ceria and doped ceria are technologically relevant materials because of the high ionic conductivity and electrocatalytic properties that make them promising materials for several industrial applications (Bellino *et al.*, 2008; Sun *et al.*, 2012; Zimicz *et al.*, 2013), and understanding the local and intermediate atomic order is key for interpreting their properties.

The XPD data are shown in Fig. S5. Fig. 8 shows the pair distribution function with $Q_{max} \simeq 20$ Å$^{-1}$ of the data collected for $CeO_2$ and nanocrystalline YDC. The PDFs for both samples are rich in well defined features and similar, but the oscillations in the nano-powder are damped with increasing $r$ owing to the finite size of the particles and vanish at ∼40 Å.

PDF refinements of the nano-YDC data using a fluorite-like structure were performed. The isotropic displacement parameters, cell constant, overall scale factor, particle size and a parameter accounting for correlated motion were allowed to vary. The plot of the fit performed over 1.5–40 Å is shown in Fig. 9(*a*). The fluorite structure fits the experimental data

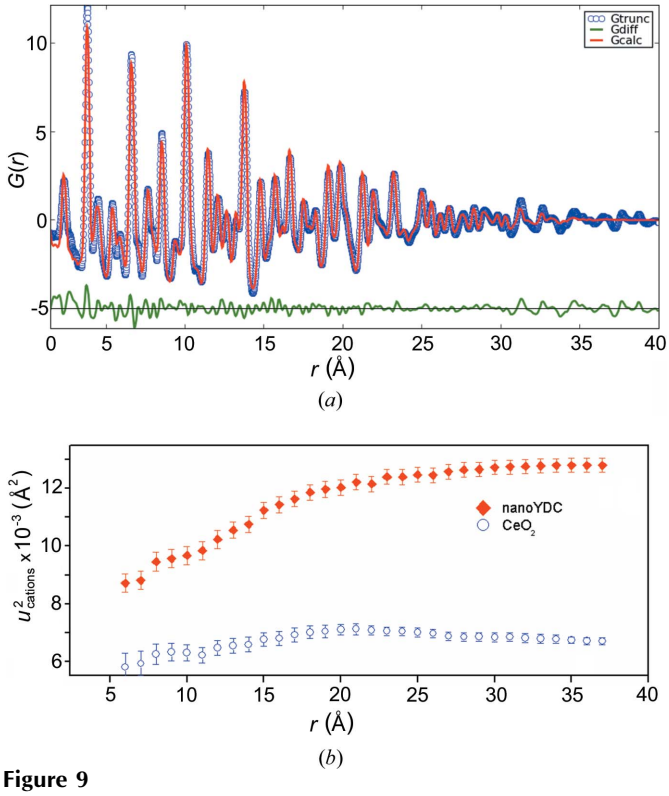


**Figure 9**
(*a*) The experimental (empty blue circles) and the calculated (solid red line) $G(r)$ for the nanocrystalline YDC sample; the difference curve is shown below (solid green line). (*b*) $u_{iso}$ obtained by a series of fits as a function of $r_{max}$ (see text for more details).

yielding a crystallite size of 4.2 nm, which is in good agreement with the size determined by the Scherrer equation using the HRPD data, and a cell parameter of 5.405 (1) Å. However, the fit shows visible discrepancies at low- and at high-$r$ regions. A series of fits of the PDF from $r_{min}$ (1.5 Å) to $r_{max}$ were performed, where $r_{max}$ was increased stepwise from 8 to 30 Å. This procedure was performed on both data sets, *i.e.* $CeO_2$ and nano-YDC; it has previously been applied for the study of systems exhibiting local or intermediate disorder and aims at investigating the length of disorder in these materials (Masadeh *et al.*, 2007; Gilbert *et al.*, 2004). The structural parameters were varied while the cluster size was fixed to 4.2 nm (as determined in the first fit over the 1.5–40 Å range) because size determination is highly correlated with other parameters. In Fig. 9(*b*) the atomic displacement factors, $u_{iso}$, of the cations obtained for nano-YDC and $CeO_2$ are plotted as a function of the $r_{max}$ used in each fit. Two observations can be extracted: first, the atomic displacement parameters of the nano-YDC are larger than those for the $CeO_2$. The presence of Y is known to affect the local atomic order, increasing the average atomic displacements in the doped samples with respect to the undoped $CeO_2$ (Coduri *et al.*, 2012). Second, while there is no abrupt change in the $u_{iso}$ of the $CeO_2$ as a function of $r$, there is an increase of the $u_{iso}$ of cations as $r$ increases. This indicates that the degree of disorder (expressed here by $u_{iso}$) depends on $r$. This is also in agreement with studies in nanostructured materials which demonstrate the presence of greater disorder with respect to the bulk material (Gilbert *et al.*, 2004; Yang *et al.*, 2013). Nevertheless, in order to understand the role of size and disorder in the structure of these solid solutions, further studies should be performed; these are beyond the scope of the present work.

**4.4.4. PDF analysis on amorphous $SiO_2$.** The final example consists of amorphous silica ($SiO_2$) glass. The three-dimensional network of $SiO_4$ tetrahedra has been extensively studied as it is important in materials science and geology. Because of the weak scattering properties and the absence of Bragg reflections it is considered as a particularly challenging sample for X-ray diffraction and PDF measurements. It has been used as a probe in the development of several PDF setups (Chupas *et al.*, 2007; Lee *et al.*, 2008; Neuefeind *et al.*, 2012).

The XPD data are shown in Fig. S7. Fig. 10 shows the $G(r)$ collected at 50 keV with $Q_{max}$ = 24.5 $Å^{-1}$. The strongest peak, observed at 1.6 Å, in the $G(r)$ function can be assigned to the Si—O bond distance, and those at 2.6 and 3.1 Å to O—O and Si—Si atomic pairs, respectively. These distances are in good agreement with data reported in the literature (Lee *et al.*, 2008; Meral *et al.*, 2011; Schulmeister & Mader, 2003). In order to emphasize the importance of collecting data at high $Q$, the inset in Fig. 10 shows PDFs of amorphous $SiO_2$ around the first peak, collected at two different wavelengths resulting in $Q_{max}$ = 20 and 24.5 $Å^{-1}$. It can be observed that, as expected, the data collected at $Q_{max}$ 24.5 $Å^{-1}$ has a better resolution in $r$ space.

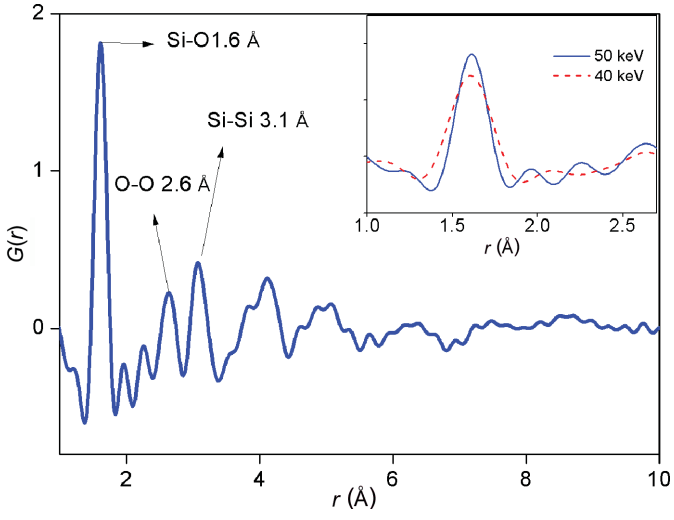


**Figure 10**
The experimental PDF for the amorphous $SiO_2$ sample where $Q_{max}$ = 24.5 $Å^{-1}$; the peaks attributed to Si—O, O—O and Si—Si distances are indicated with arrows. Inset: comparison of the data collected at different energies.

### 4.5. Data collection time and *in situ* capabilities

Important structural information can be gained in industrially relevant materials under their real working conditions using *in situ* and *operando* setups. The SNBL is providing several cells and equipment for this purpose. Owing to the dynamic changes in the materials during operation, time resolution is an important parameter to consider. The minimum time to acquire a good quality diffraction pattern depends on several variables: for example, the sample composition (atomic scattering factor), its crystallinity, the incoming X-ray flux and the quality of the detector system.

As an illustrative example of the *in situ* capabilities of this detector the $\beta/\gamma \rightarrow \alpha$ phase transition in silver iodide (Johan *et al.*, 2011) was monitored as a function of temperature and time. Fig. 11 shows the evolution with time and temperature of the XPD data collected on AgI powder during a heating cycle

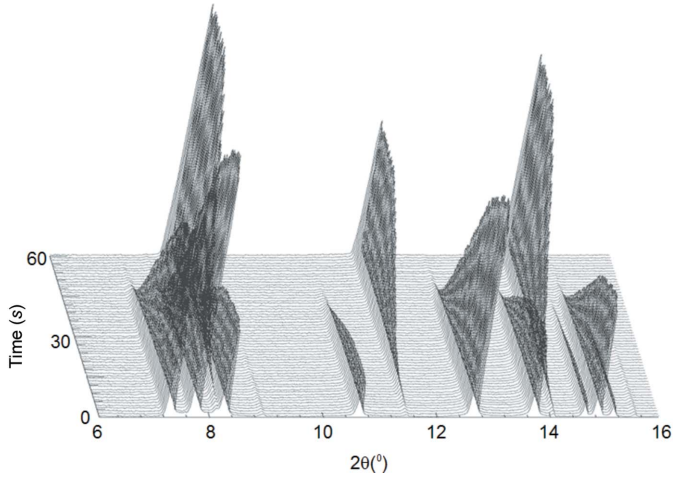


**Figure 11**
Background-subtracted XPD data as a function of time (60 s shown here), collected upon heating at a rate of 120 K $h^{-1}$.

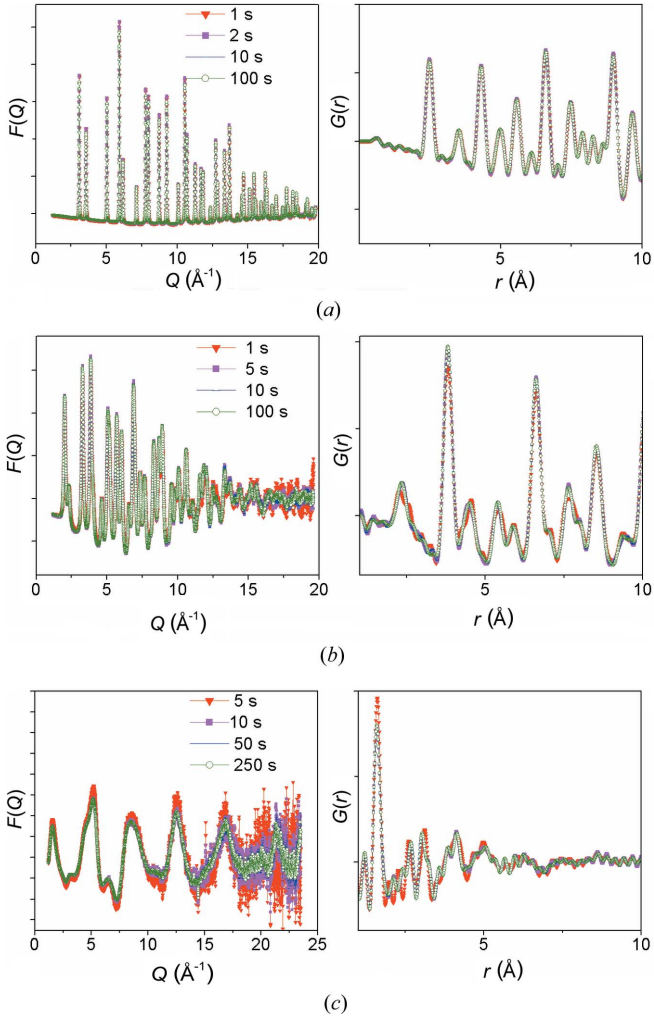


**Figure 12**
The reduced scattering function $F(Q)$ and the PDF $G(r)$ collected with different acquisition times for (*a*) Ni, (*b*) nano-YDC and (*c*) amorphous $SiO_2$.

at a rate of 120 K $h^{-1}$ (between 417 and 419 K) and a time resolution of 1 s per image. The phase change occurred, in this case, in around 60 s; the plot in Fig. 11 shows that it is possible to monitor kinetics at such high speeds with sufficient sampling.

On the other hand, PDF analysis normally requires longer recording times than conventional XPD analysis. For the examples considered above the quality of the data as a function of time was examined. Fig. 12 shows the $F(Q)$ and $G(r)$ functions collected with different acquisition times for samples with different crystallinity: Ni, nano-YDC and amorphous $SiO_2$. In all cases, the signal-to-noise ratio in $F(Q)$ is improved with the acquisition time. This becomes more evident when decreasing the crystallinity from Ni to amorphous $SiO_2$. Nevertheless, the $G(r)$ features are already very clear at 1 s for the case of Ni, whereas nano-YDC and amorphous $SiO_2$ need 5 and 10 s each, respectively, to reach a similar quality. Fig. 13 shows the residuals of fits performed on different $G(r)$ functions as a function of acquisition time for (*a*) nano-YDC and (*b*) Ni. These plots indicate that there is no further improvement above 50 and 100 s for the Ni and nano-YDC samples, respectively. Thus, the quality of the data does not improve further for acquisition times longer than 50 and 100 s for these two samples, and it is hence defined by the experimental setup and the nature of the samples.

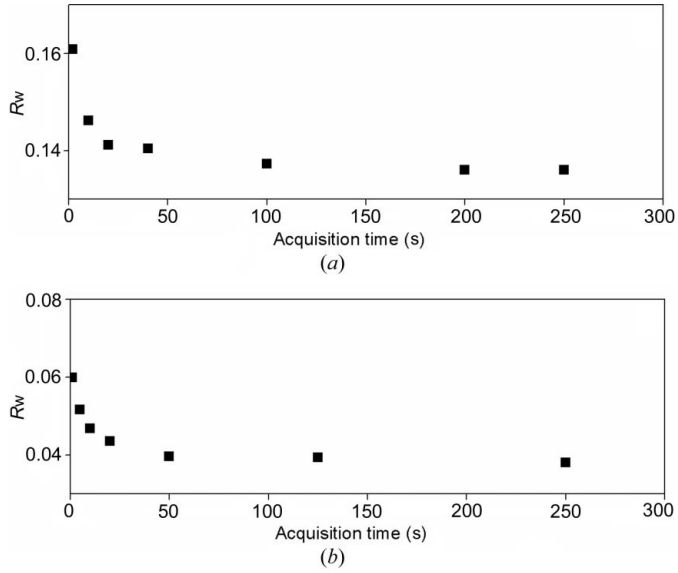


**Figure 13**
Residual of the fits, $R_w$, performed with different acquisition time data collected on (*a*) nano-YDC and (*b*) Ni samples (fits performed in the range of 1.5–20 Å).

## 5. Conclusions

A large-area CMOS detector has been tested in synchrotron powder diffraction experiments. Rietveld refinements were performed on data from an $LaB_6$ NIST powder standard collected at different energies. The normalized extracted intensities from the X-ray powder diffraction data are independent of the X-ray energy (between 20 and 50 keV) and in agreement with published data as well as HRPD data collected on the same sample. PDF analysis with a medium real-space resolution ($Q_{max}$ = 20–24.5 $Å^{-1}$) was successfully performed on microcrystalline nickel, nanocrystalline yttrium-doped ceria and amorphous $SiO_2$. The capabilities of the detector system for time-resolved experiments have been evaluated by following the $\beta/\gamma \rightarrow \alpha$ phase transition in AgI down to 1 s per image. Further developments could come from a better cooling system, reducing dark noise and improving stability to enable easier operational procedures. The current results clearly show that this detector provides exciting opportunities for high-energy and time-resolved X-ray scattering experiments.

The authors thank Roberto Homs and Staffan Ohlsson (ESRF) for their excellent computing support and for getting the detector system up and running. Sebastien Petitdemange and Jerome Kieffer (ESRF) are thanked for the development and implementation of the LIMA interface and *pyFAI* soft-

ware, respectively, as well as for great teamwork; Hermann Emerich and Vladimir Dmitriev for support (SNBL) and Dmitry Chernyshov (SNBL) for being able to always come up with valuable suggestions to answer our questions; Magnus Rønning, Atsushi Urakawa and the Research Council of Norway for funding of the detector through Synknøyt proposal 21840; and Diego G. Lamas for his contribution on the nanocrystalline sample. HM thanks the Research Council of Norway for funding through Synknøyt proposal 21849.

## References

Beek, W. van, Safonova, O. V., Wiker, G. & Emerich, H. (2011). *Phase Transitions*, **84**, 726–732.
Bellino, M. G., Lamas, D. G. & Walsöe de Reca, N. E. (2008). *J. Mater. Chem.* **18**, 4537–4542.
Billinge, S. J. L. (2010). *Physics*, **3**, 25.
Booth, C. H., Sarrao, J. L., Hundley, M. F., Cornelius, A. L., Kwei, G. H., Bianchi, A. & Lawrence, J. M. (2001). *Phys. Rev. B*, **63**, 224302.
Chupas, P. J., Chapman, K. W. & Lee, P. L. (2007). *J. Appl. Cryst.* **40**, 463–470.
Chupas, P. J., Qiu, X., Hanson, J. C., Lee, P. L., Grey, C. P. & Billinge, S. J. L. (2003). *J. Appl. Cryst.* **36**, 1342–1347.
Coduri, M., Brunelli, M., Scavini, M., Allieta, M., Masala, P., Capogna, L., Fischer, H. E. & Ferrero, C. (2012). *Z. Kristallogr.* **227**, 272–279.
Coelho, A. A. (2007). *TOPAS-Academic.* Version 4.1. Coelho Software, Brisbane, Australia.
Egami, T. & Billinge, S. J. L. (2003). *Underneath the Bragg Peaks: Structural Analysis of Complex Materials*. Amsterdam: Elsevier.
Farrow, C. L., Juhàs, P., Liu, J. W., Bryndin, D., Bozin, E. S., Bloch, J., Proffen, T. & Billinge, S. J. L. (2007). *J. Phys. Condens. Matter*, **19**, 335219.
Gilbert, B., Huang, F., Zhang, H., Waychunas, G. A. & Banfield, J. F. (2004). *Science*, **305**, 651–654.
Graeve, T. & Weckler, G. P. (2001). *Proc. SPIE*, **4320**, 68–76.
Hammersley, A. P. (1998). *FIT2D V9.129* Reference Manual, V3.1. Internal Report ESRF98HA01T. ESRF, Grenoble, France. http://www.esrf.fr/computing/scientific/FIT2D/.
Hasegawa, K., Hirata, K., Shimizu, T., Shimizu, N., Hikima, T., Baba, S., Kumasaka, T. & Yamamoto, M. (2009). *J. Appl. Cryst.* **42**, 1165–1175.
Homs, A., Claustre, L., Kirov, A., Papillon E. & Petitdemange, S. (2011). Proceedings of ICALEPS2011, Grenoble, France, p. 676.
Hong, X., Chen, Z. & Duffy, T. S. (2012). *Rev. Sci. Instrum.* **83**, 063901.
Johan, M. R., Leng, T. S., Hawari, N. L. & Suan, S. (2011). *Int. J. Electrochem. Sci.* **6**, 6236–6243.
Juhás, P., Davis, T., Farrow, C. L. & Billinge, S. J. L. (2013). *J. Appl. Cryst.* **46**, 560–566.
Kieffer, J. & Karkoulis, D. (2013). *J. Phys. Conf. Ser.* **425**, 202012.
Kieffer, J. & Wright, J. P. (2013). *Powder Diffr.* **28**, 339–350.
Korsukova, M. M., Lundstroem, T., Gurin, V. N. & Tergenius, L. E. (1984). *Z. Kristallogr.* **149**, 299–306.
Kraft, P., Bergamaschi, A., Broennimann, Ch., Dinapoli, R., Eikenberry, E. F., Henrich, B., Johnson, I., Mozzanica, A., Schlepütz, C. M., Willmott, P. R. & Schmitt, B. (2009). *J. Synchrotron Rad.* **16**, 368–375.
Labiche, J., Mathon, O., Pascarelli, S., Newton, M. A., Ferre, G. G., Curfs, C., Vaughan, G., Homs, A. & Carreiras, D. F. (2007). *Rev. Sci. Instrum.* **78**, 091301.
Lee, J. H., Aydıner, C. C., Almer, J., Bernier, J., Chapman, K. W., Chupas, P. J., Haeffner, D., Kump, K., Lee, P. L., Lienert, U., Miceli, A. & Vera, G. (2008). *J. Synchrotron Rad.* **15**, 477–488.
Masadeh, A. S., Božin, E. S., Farrow, C. L., Paglia, G., Juhas, P. & Billinge, S. J. L. (2007). *Phys. Rev. B*, **76**, 115413.
Meral, C., Benmore, C. J. & Monteiro, P. J. M. (2011). *Cem. Concr. Res.* **41**, 696–710.
Neuefeind, J., Feygenson, M., Carruth, J., Hoffmann, R. & Chipley, K. K. (2012). *Nucl. Instrum. Methods Phys. Res. Sect. B*, **287**, 68–75.
Ponchut, C. (2006). *J. Synchrotron Rad.* **13**, 195–203.
Rodriguez-Carvajal, J. (2001). IUCr Commission on Powder Diffraction Newsletter, No. 26, pp. 12–19.
Rouquette, J., Haines, J., Fraysse, G., Al Zein, A., Bornand, V., Pintard, M., Papet, P., Hull, S. & Gorelli, F. A. (2008). *Inorg. Chem.* **47**, 9898–9904.
Ruat, M. & Ponchut, C. (2012). *IEEE Trans. Nucl. Sci.* **59**, 2392–2401.
Schulmeister, K. & Mader, W. (2003). *J. Non-Cryst. Solids*, **320**, 143–150.
Sun, C., Li, H. & Chen, L. (2012). *Energy Environ. Sci.* **5**, 8475–8505.
Yagi, N. & Inoue, K. (2007). *J. Appl. Cryst.* **40**, s439–s441.
Yang, X., Masadeh, A. S., McBride, J. R., Bozin, E. S., Rosenthal, S. J. & Billinge, S. J. L. (2013). *Phys. Chem. Chem. Phys.* **15**, 8480–8486.
Zimicz, M. G., Núñez, P., Ruiz-Morales, J. C., Lamas, D. G. & Larrondo, S. A. (2013). *J. Power Sources*, **238**, 87–94.